

ARTICLE

Received 15 Aug 2014 | Accepted 29 Oct 2014 | Published 15 Dec 2014

DOI: 10.1038/ncomms6710

# Spatial control of functional properties via octahedral modulations in complex oxide superlattices

E.J. Moon<sup>1</sup>, R. Colby<sup>2,†</sup>, Q. Wang<sup>3</sup>, E. Karapetrova<sup>4</sup>, C.M. Schlepütz<sup>4</sup>, M.R. Fitzsimmons<sup>3</sup> & S.J. May<sup>1</sup>

Control of atomic structure, namely the topology of the corner-connected metal-oxygen octahedra, has emerged as an important route to tune the functional properties at oxide interfaces. Here we investigate isovalent manganite superlattices (SLs),  $[(\text{La}_{0.7}\text{Sr}_{0.3}\text{MnO}_3)_n/(\text{Eu}_{0.7}\text{Sr}_{0.3}\text{MnO}_3)] \times m$ , as a route to spatial control over electronic bandwidth and ferromagnetism through the creation of octahedral superstructures. Electron energy loss spectroscopy confirms a uniform Mn valence state throughout the SLs. In contrast, the presence of modulations of the  $\text{MnO}_6$  octahedral rotations along the growth direction commensurate with the SL period is revealed by scanning transmission electron microscopy and X-ray diffraction. We show that the Curie temperatures of the constituent materials can be systematically engineered via the octahedral superstructures leading to a modulated magnetization in samples where the SL period is larger than the interfacial octahedral coupling length scale, whereas a single magnetic transition is observed in the short-period SLs.

<sup>1</sup>Department of Materials Science and Engineering, Drexel University, 3141 Chestnut Street, 344 LeBow Engineering Building, Philadelphia, Pennsylvania 19104, USA. <sup>2</sup>Environmental Molecular Sciences Laboratory, Pacific Northwest National Laboratory, Richland, Washington 99352, USA. <sup>3</sup>Lujan Neutron Scattering Center, Los Alamos National Laboratory, Los Alamos, New Mexico 87545, USA. <sup>4</sup>X-ray Science Division, Advanced Photon Source, Argonne National Laboratory, Argonne, Illinois 60439, USA. † Present address: ExxonMobil Research and Engineering Company, Annandale, New Jersey 08801, USA. Correspondence and requests for materials should be addressed to E.J.M. (email: em582@drexel.edu) or to S.J.M. (email: smay@coe.drexel.edu).

Interfaces between dissimilar complex oxides provide an exciting platform to design, confine and control physical properties in a class of materials that exhibits ferroic orderings, correlated electron behaviour and strong coupling between electronic, ionic, orbital, spin and lattice degrees of freedom<sup>1</sup>. A central goal within this field is to identify the length scales over which interfacial reconstructions alter behaviour and use this knowledge to design spatially confined or modulated properties. For example, electronic reconstructions at heterointerfaces have received considerable experimental and theoretical interest revealing a length scale of a few unit cells for charge transfer between heterovalent or elementally distinct cations<sup>2–9</sup>, enabling delta-doping strategies to spatially tailor electronic and magnetic behaviour<sup>10–13</sup>. More recently, exploiting the structural coupling at  $ABO_3$  perovskite interfaces has been recognized as a route for engineering functional properties<sup>14–16</sup>. One structure-driven approach is to utilize non-bulk-like distortions or rotations of the corner-connected  $BO_6$  octahedra across interfaces in which the two constituent materials exhibit either a different pattern and/or magnitude of octahedral rotations. Given the strong coupling between octahedral rotations and electronic/ferroic properties—increasing the magnitude of rotations tends to localize carriers and reduce magnetic ordering temperatures<sup>17–19</sup>—a local enhancement or suppression of rotations provides a means to induce new electronic, ferroelectric or magnetic behaviour. In particular, the electronic bandwidth ( $W$ ) is given as  $W \propto \cos \omega/d^{3.5}$ , where  $\omega$  is  $\frac{1}{2}(\pi - \theta)$ ,  $\theta$  is the  $B-O-B$  bond angle and  $d$  is the  $B-O$  bond length, and has been used to correlate electronic and magnetic behaviour with structural changes in bulk manganites and other perovskites<sup>18,20</sup>. Although interfacial octahedral coupling has been shown to alter  $\theta$  over roughly 2–8 unit cells (uc) on either side of a heterojunction<sup>21–26</sup>, the explicit use of this length scale to tune between uniform or modulated behaviour in oxide heterostructures has yet to be explored.

In this work, we demonstrate spatial control over electronic bandwidth and ferromagnetism through the creation of octahedral superstructures in isovalent manganite superlattices (SLs). By varying the SL period relative to the interfacial octahedral coupling length scale, we demonstrate that there is a transition from a modulated magnetization in large-period SLs to a more uniform magnetization in short-period SLs. Controlling the structural modulation at the intermediate length scales allows for the systematic tuning of the constituent materials' Curie temperatures. The fixed valence state of the Mn cations and the choice of SL periods ensure that the observed magnetic properties are driven by octahedral coupling and not charge transfer or

strain. The implications of the work extend well beyond magnetic manganites, as these results highlight the promise of tailoring and spatially confining electronic and ferroic behaviour in oxide heterostructures through the design of rotational gradients or structural delta doping approaches.

## Results

**SL design.** Octahedral superstructures are realized in  $[(La_{0.7}Sr_{0.3}MnO_3)_n/(Eu_{0.7}Sr_{0.3}MnO_3)_n] \times m$  SLs grown on  $(La_{0.3}Sr_{0.7})(Al_{0.65}Ta_{0.35})O_3$  (LSAT) substrates, where  $n$  is in uc.  $La_{0.7}Sr_{0.3}MnO_3$  (LSMO) and  $Eu_{0.7}Sr_{0.3}MnO_3$  (ESMO) are iso-electronic compounds, in which differences in physical properties arise because of atomic structure. In particular, rotations of the  $MnO_6$  octahedra lead to average Mn–O–Mn bond angles ( $\theta$ ) of  $166.3^\circ$  and  $157^\circ$  in bulk LSMO and ESMO, respectively, giving rise to larger electronic bandwidth in LSMO compared with ESMO<sup>18,27</sup>. As a result, LSMO is a ferromagnetic metal with a  $T_C$  of 370 K, whereas bulk ESMO is a ferromagnetic insulator with  $T_C$  less than 100 K (refs 28,29). Deposited on LSAT, ESMO and LSMO are subjected to  $<0.6\%$  tensile and  $<0.2\%$  compressive strain, respectively. This strain will alter the exact magnitude of the ESMO and LSMO bond angles compared with their bulk counterparts; however, the average bond angles in ESMO on LSAT will still be less than that of LSMO on LSAT because of differences in the A-site cationic size. When epitaxially joined in SLs (Fig. 1a), the atomic structure in the ESMO and LSMO layers will depend on the SL period ( $2n$ ) and the length scale for interfacial coupling of octahedral rotations ( $\xi_\theta$ ). If the layer thickness is greater than  $\xi_\theta$ , then the non-interfacial regions of LSMO and ESMO will exhibit differences in rotation angle because of their differences in bulk structure ( $\Delta\theta = \theta_{LSMO} - \theta_{ESMO}$ ). However, as the interfaces are brought closer together, making  $\xi_\theta$  comparable to or greater than  $n$ , the structure of the layers will be increasingly dictated by the interfacial octahedral coupling, reducing the magnitude of  $\Delta\theta$ . Thus, by tuning  $n$ , one can control the amplitude and period of octahedral modulations in the heterostructures. Octahedral modulation in the SLs will produce modulations of  $W$  (Fig. 1b), and functional properties dependent on  $W$ , such as magnetic exchange and electronic conduction. We note that changes to  $\theta$  also modify  $d$ ; for a fixed in-plane lattice parameter,  $d$  will increase as  $\theta$  is reduced. Both effects, a reduction in  $\theta$  and an increase in  $d$ , reduce  $W$ . The design and control of octahedral modulations thus provide a unique opportunity to spatially confine functional behaviour in perovskite oxides without relying on charge transfer.

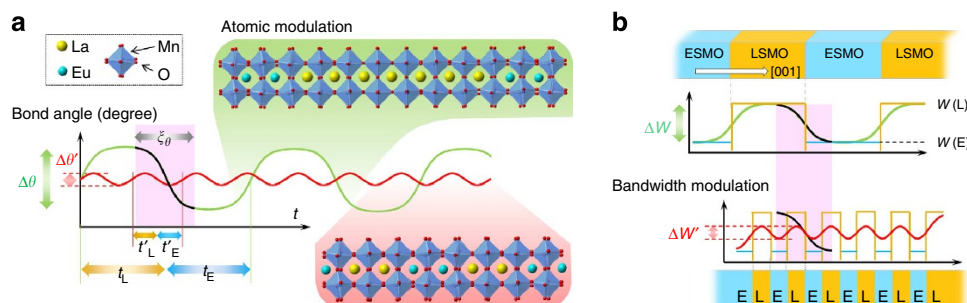


**Figure 1 | Schematic of atomic and electronic modulations.** (a) Changes of bond angle ( $\Delta\theta$  in green) along growth direction across a  $(t_L + t_E) \times m$  superlattice composed of LSMO and ESMO, where  $t_L$  is the LSMO layer thickness and  $t_E$  is the ESMO layer thickness. One segment of the bond angle modulation is shown in the upper panel. The red oscillating line in the centre panel illustrates behaviour when the layer thickness is less than the interfacial structural coupling length scale ( $\xi_\theta$ , in black line) corresponding to a superlattice structure shown in the lower panel.  $t'$  indicates the layer thickness in the short-period superlattice. (b) The accompanying changes to electronic bandwidth ( $W$ ) are illustrated for a large-period superlattice (top panel) and short-period superlattice (bottom panel).

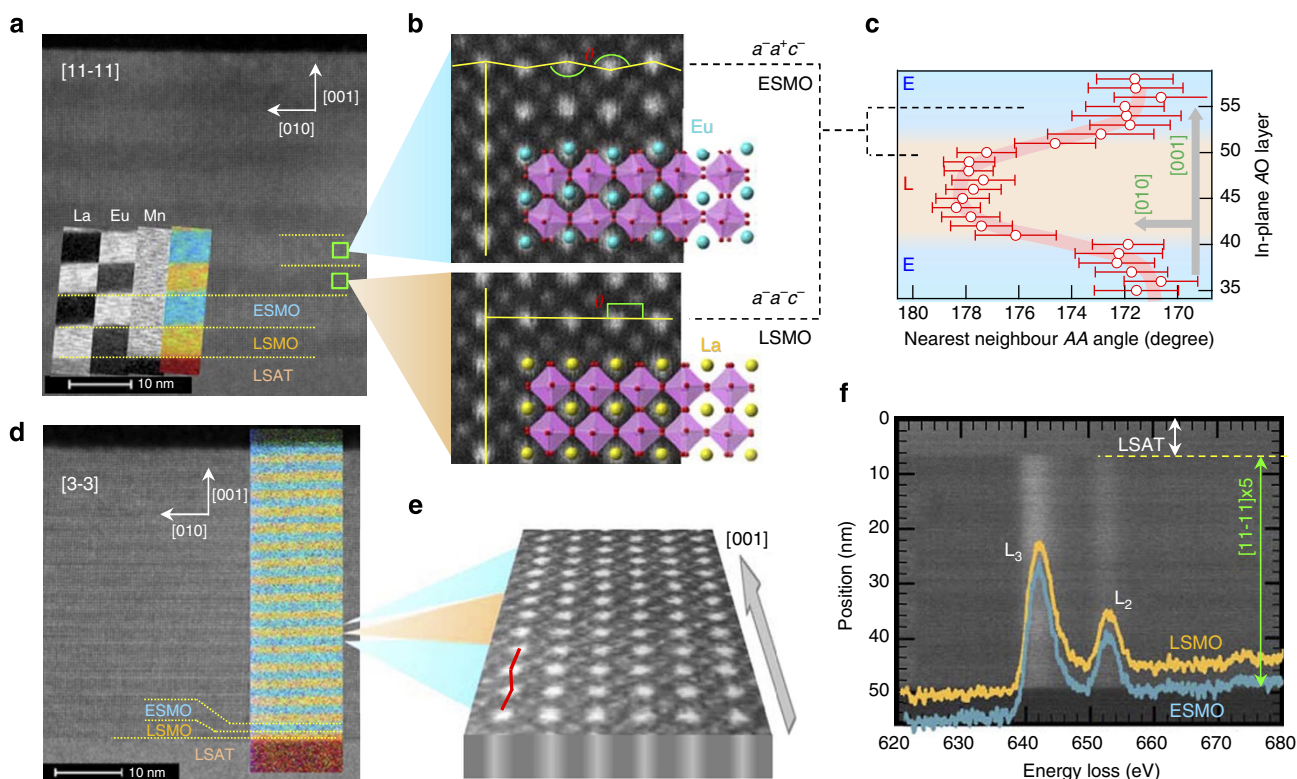
**Scanning transmission electron microscopy.** Electron energy loss spectroscopy (EELS) and scanning transmission electron microscopy (STEM) were used to confirm the presence of structural modulations tuned by the SL period. Figure 2a displays a high-angle annular dark field (HAADF)-STEM image of a  $n = 11$  SL viewed from the  $[100]$  direction of LSAT. The SL is epitaxial across interfaces and uniform over a large area. The LSMO layers appear darker and the ESMO brighter because of the higher Z of Eu compared with La. The different intensity between LSMO and ESMO layers provides a good indication of the minimal interfacial roughness. Furthermore, the sharpness of the La and Eu EELS profiles across the SL further confirms that the LSMO and ESMO layers are well defined (inset of Fig. 2a).

Figure 2b shows high-magnification HAADF-STEM images of non-interfacial ESMO (top) and LSMO layers (bottom) in the  $n = 11$  SL, enlarged from the green boxes in Fig. 2a. In these images, atomic columns of A-site cations (for example,  $\text{La}_{0.7}\text{Sr}_{0.3}$  or  $\text{Eu}_{0.7}\text{Sr}_{0.3}$ ) are clearly resolved so that A-site displacements can be discerned<sup>30</sup>. In bulk form, ESMO exhibits the  $a^-a^+c^-$  rotation pattern with A-site displacements within the (010) plane, whereas LSMO exhibits the  $a^-a^-c^-$  rotation pattern, which lacks A-site displacements. The notation that defines the rotation pattern is such that a superscript, appended to each axis, indicates whether neighbouring octahedra rotate in-phase (+), out-of-phase (-) or if rotations are absent (0)<sup>31–33</sup>. Note that in bulk orthorhombic perovskites, the A-site displacements lie in the plane perpendicular to the

in-phase rotation axis. As shown in the upper panel of Fig. 2b for the non-interfacial ESMO layers, the A-site atoms are displaced within the (0 1 0) plane, consistent with an  $a^-a^+c^-$  rotation pattern. On the other hand, the non-interfacial LSMO does not exhibit A-site displacements, consistent with the bulk LSMO structure.

To quantitatively analyse the octahedral connections across the heterointerface, we measured the A–A–A angle for the  $n = 11$  SL. The A-site positions were determined from HAADF images of each layer and the angle between three successive A-site atoms along the  $[010]$  direction was used to quantify the A-site displacements. Previous work has shown that these A-site angles provide a relative measure of the B–O–B bond angles ( $\theta$ )<sup>24</sup>. Figure 2c presents the variations of the A-site displacement angles across ESMO/LSMO interfaces; the non-interfacial region of the LSMO layer exhibits negligible A-site displacements, whereas the non-interfacial ESMO regions have angles reduced by  $\sim 10^\circ$ . In the interfacial region, the A-site angles vary smoothly between LSMO and ESMO over  $\sim 4$  uc.

An HAADF-STEM image of the  $n = 3$  SL is shown in Fig. 2d, exhibiting well-defined ESMO and LSMO layers confirmed by the EELS colour map as shown inset (La in yellow and Eu in blue). A perspective view of a high-magnification HAADF-STEM image is shown, to help highlight the A-displacement, in Fig. 2e. In the ESMO layers, A-site displacements are present within the (001) plane. This behaviour is orthogonal to that observed in the  $n = 11$  SL, where the A-site displacements occurred within the (010)



**Figure 2 | Atomic structure of the superlattices.** (a) HAADF-STEM image of  $[n = 11] \times 5$  SL grown on LSAT. Inset shows an EELS map (La in orange, Eu in blue). (b) Enlarged HAADF-STEM images from typical LSMO (orange) and ESMO (blue) layers showing A-site displacements ( $A = \text{La}_{0.7}\text{Sr}_{0.3}$  or  $\text{Eu}_{0.7}\text{Sr}_{0.3}$ ), highlighted with the yellow line. A schematic of the crystal structure is superimposed. (c) A-site displacement angles measured between three successive A-site columns (adjacent AO layers) along  $[010]$  direction. The orange and blue areas indicate LSMO and ESMO layers, respectively. The error bars represent 0.5 multiplied by the standard deviation of the mean of the A-site displacement angle obtained from image analysis. (d) HAADF-STEM image of the  $[n = 3] \times 17$  SL grown on LSAT. Inset shows an EELS map. (e) Perspectively enlarged HAADF-STEM images from three adjacent ESMO/LSMO layers showing A-site displacements across the SL interfaces. (f) EELS profile for the Mn L-edge from the  $n = 11$  SL with superimposed averaged Mn L-edge spectra for the non-interfacial regions of the ESMO and LSMO. The Mn  $L_{2,3}$  edge positions and shapes are consistent throughout the SL indicating a constant nominal Mn valence state across the LSMO/ESMO layers.

plane. In contrast to the  $n = 11$  SL, the structure of the  $n = 3$  SL does not modulate strongly throughout the SL.

The spectrum of the Mn L-edge is used to characterize the Mn valence along the growth direction using EELS. Figure 2f shows a plot of the Mn L-edge as a function of depth and energy across the  $n = 11$  SL (shown without background compensation, to help highlight the positions of the ESMO and LSMO layers). Also shown are corresponding averaged spectra from the non-interfacial regions of the LSMO and ESMO layers (with background compensation). The Mn  $L_{2,3}$ -edge represents transitions from  $2p_{1/2}$  to  $2p_{3/2}$  states to the unfilled 3d states. Importantly, the spectra exhibit no obvious shift or changes in the shape of the Mn L-edge from ESMO to LSMO layers throughout the SL. This indicates a homogeneous mixed Mn valence state across the SL without charge transfer at the heterointerfaces, confirming that physical properties described later arise from structural modulations and not charge-based effects. Finally, we note that the EELS measurements from the  $n = 11$  SL indicate a length scale of 3–4 uc for La/Eu intermixing at the interfaces, as shown in Supplementary Fig. 1.

**Synchrotron X-ray scattering.** Synchrotron X-ray diffraction (XRD) provides further evidence of the interfacial integrity of the SLs and allows for measurement of the octahedral behaviour within the samples. Figure 3a shows synchrotron diffraction measurements along the  $(0\ 0\ L)$  truncation rod of the  $n = 3, 6$  and 11 SLs. Satellite peaks are observed for all SLs, confirming that the LSMO and ESMO layers form a cation-ordered superstructure.

The measured data are in agreement with simulations (red solid lines), obtained using the GenX programme<sup>34</sup>, in which the SL is modelled as perfectly crystalline with atomically abrupt interfaces. In the simulation, the numbers of unit cells for both LSMO and ESMO were fixed to  $n = 3, 6$  and 11. The calculated diffraction results shown in Fig. 3a were obtained using  $c$ -axis parameters of 3.879, 3.890 and 3.892 (3.803, 3.828 and 3.836) Å for the LSMO (ESMO) for  $n = 3, 6, 11$ , respectively.

Although analysis of half-order peak intensities can be used to quantify bond angles in perovskite SLs<sup>35</sup>, this procedure is not possible in the present SLs because of the overlapping signal from the film and the intense peaks from the LSAT substrate. However, satellite peaks off of the  $(1/2\ 1/2\ 3/2)$  peaks along  $L$  were measured for the SLs. These satellite peaks arise from modulations of the amplitude of the octahedral rotations along the growth direction. For instance, in Fig. 3b, a satellite peak is visible near  $L = 1.66$  for the  $n = 3$  SL. For the  $n = 3$  and 6 SLs, the distance between the  $(1/2\ 1/2\ 3/2)_{SL}$  peak and the first SL satellite peaks is  $\Delta L \sim 1/6$  and  $1/12$ ; similarly, for the  $n = 11$  SL, the  $\Delta L$  between adjacent satellite peaks is  $1/22$ . The presence of these satellite peaks at these positions in momentum space confirms that the period of the rotational superstructure is the same as the compositional period of the SLs, consistent with the scenario presented in Fig. 1a.

In addition to confirming the presence of rotational modulations, measurement of the half-order peaks were used to identify the dominant rotation pattern present in each SL. As shown in Fig. 3c, half-order  $(1/2\ 3/2\ 1)$  reflections were observed only in the  $n = 3$  and 6 samples. The presence of this peak indicates an

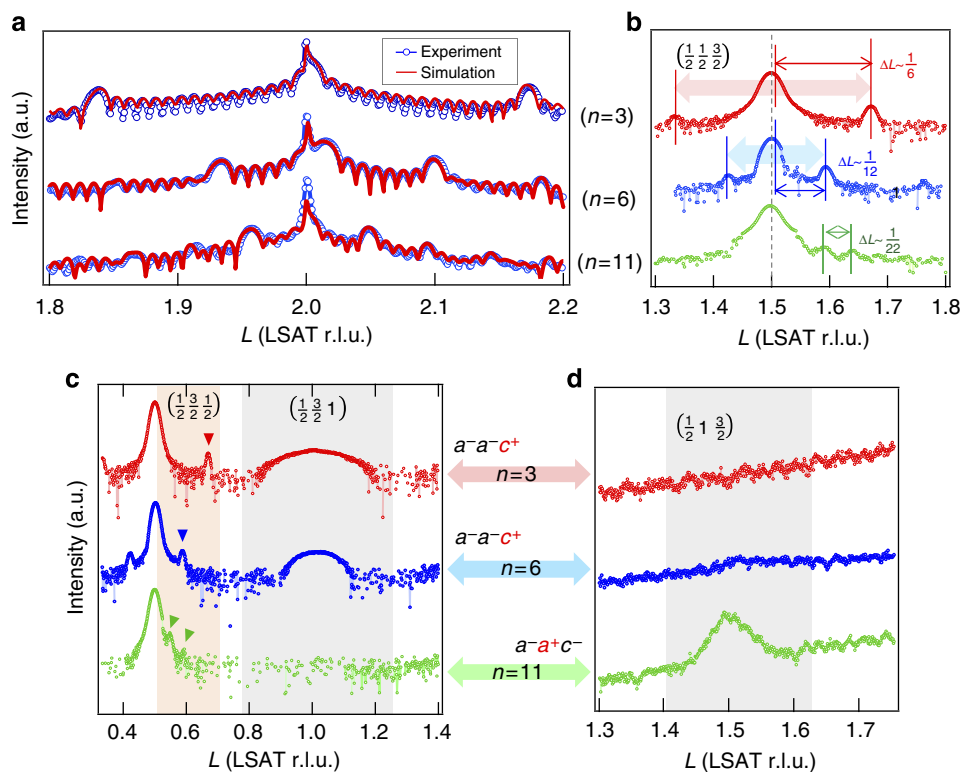


**Figure 3 | Synchrotron X-ray diffraction.** (a) Diffraction data along the  $(00L)$  in three SL films,  $n = 3, 6$  and 11 from top, grown on LSAT substrates exhibiting distinct satellite peaks because of the coherent SL structure. Red lines show the corresponding simulations; r.l.u. stands for reciprocal lattice units. (b) Half-order satellite peaks near the  $(1/2\ 1/2\ 3/2)_{SL}$  reflection arising from modulations in the amplitude of the octahedral rotations along the growth direction. The distance between two satellite peaks ( $\Delta L$ ) confirms the period of the octahedral superstructure is the same as the chemical period of the superlattice. The LSAT substrate exhibits a broad, intense  $(1/2\ 1/2\ 3/2)$  peak, which obscures the principle  $(1/2\ 1/2\ 3/2)$  peak from the superlattice. (c) The  $(1/2\ 3/2\ 1)_{SL}$  reflection is observed in  $n = 3$  and  $n = 6$  SLs, indicating the presence of a  $a^-a^-c^+$  rotation pattern. (d) The  $(1/2\ 1\ 3/2)_{SL}$  reflection is observed only in  $n = 11$  SL, indicating a  $a^-a^+c^-$  pattern. The results in c and d are consistent with the direction of A-site displacements shown in Fig. 2b,e.

$a^- a^- c^+$  rotation<sup>32</sup>, a result consistent with the A-site displacements observed in the STEM imaging. In addition, the widths of these peaks along  $L$  yield correlation lengths that increase with increasing  $n$ . However, the magnitude of the correlations lengths are slightly less than  $2n$ , indicating that in-phase rotations and A-site displacements that produce the  $(1/2 \ 3/2 \ 1)$  peak are not correlated through the SL but instead are only coherent within each ESMO layer. In contrast, the  $n=11$  SL exhibits a  $(1/2 \ 1 \ 3/2)$  peak, as shown in Fig. 3d. This peak is indicative of an  $a^- a^+ c^-$  rotation pattern, again consistent with the STEM imaging presented in Fig. 2b.

**Polarized neutron reflectivity (PNR).** To determine the effect of the octahedral modulations on ferroic behaviour, the magnetic depth profile of the  $n=11$  SL was obtained using PNR. The PNR data measured at 5, 60 and 100 K are shown in Fig. 4a–c, respectively. The magnetic depth profile was obtained by fitting the PNR data using the NIST Refl1D software package<sup>36</sup>. In the fits, the nuclear scattering length densities for both LSMO and

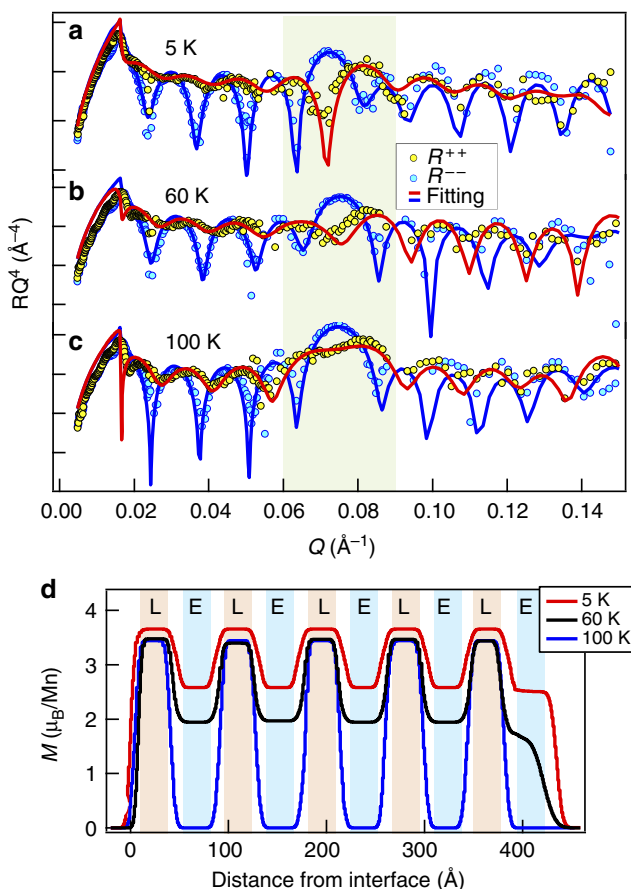


**Figure 4 | Magnetic depth profile obtained from PNR.** Reflectivity multiplied by  $Q^4$  from the  $n=11$  SL obtained at (a) 5 K, (b) 60 K and (c) 100 K, measured with a 5,000-Oe field in-the-plane of the films. Yellow and blue symbols (experimental data) indicate the reflectivity obtained with neutrons polarized parallel ( $R^{++}$ ) and antiparallel ( $R^{--}$ ) to the sample magnetization, respectively. The green enclosed box highlights the SL Bragg peak. (d) Magnetic depth profiles of the SL film corresponding to each temperature. Orange and blue regions indicate the LSMO and ESMO layers, respectively. The white regions in between LSMO and ESMO regions indicate the interfacial regions. The magnetic depth profile reveals an independent Curie temperature below 100 K within the ESMO layers in the SL.

ESMO were fixed to  $3.5 \times 10^{-6}$  and  $3.4 \times 10^{-6} \text{ \AA}^{-2}$ , consistent with their calculated values, while allowing the magnetization and the thickness of the LSMO and ESMO layers to vary in order to optimize the fit. The fitting parameters were also restricted to ensure that the magnetization did not exceed  $\sim 3.7 \mu_B$  per Mn anywhere in the structure, which is the saturation magnetization of bulk LSMO. In addition to the ESMO and LSMO layers, an interfacial layer was used. The magnetization and thickness of the interfacial layer were allowed to vary. All interfacial layers were constrained to have the same magnetization and thickness, resulting in interfacially symmetric profiles. The magnetization in the surface layers of the ESMO and the LSMO layers directly adjacent to the LSAT substrate was free to differ from the rest of the SL. This set of constraints produces good fits to the data, shown by the solid lines in Fig. 4a–c, yielding a magnetic structure in which a larger magnetization is observed in the LSMO layers compared with the ESMO layers at 5 K. As the temperature is increased, the magnetization in the ESMO is suppressed and finally negligible at 100 K. In contrast, the magnetization in the LSMO layers exhibits little change from 5 to 100 K. The magnetic depth profiles, obtained from the PNR fits, confirm that the LSMO and ESMO layers act as magnetically distinct materials in the  $n=11$  SL, as would be expected for a sample where the octahedral rotations in LSMO and ESMO differ markedly. Interestingly, the thickness of the interfacial magnetic regions across the manganite heterojunctions is  $\sim 15 \text{ \AA}$ , in good agreement with the thickness of the interfacial regions with varying A-site displacement angles obtained from STEM analysis (Fig. 2c).

**Magnetization.** To better understand the evolution of the magnetization ( $M$ ) as the interfacial density is increased in going from  $n=11$  to 3, vibrating sample magnetometry measurements were carried out. Figure 5a shows the magnetization of each SL film as a function of temperature under a magnetic field of 500 Oe. Although all three SLs were similar in total thickness ( $\sim 100 \text{ uc}$ )

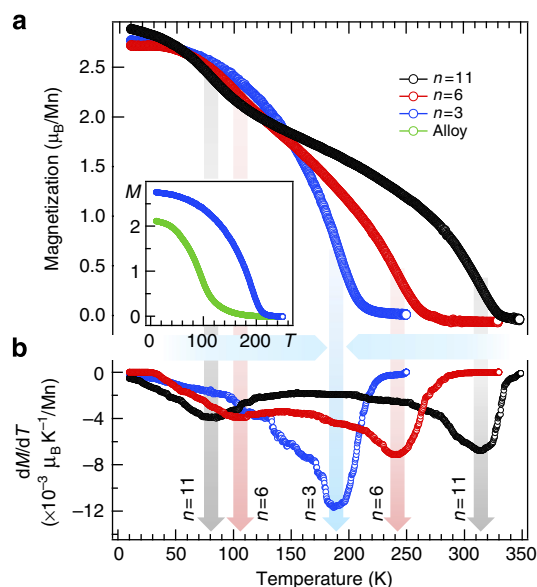


**Figure 5 | Magnetization measurements of three SLs.** (a)  $M$ - $T$  under a 500-Oe field applied in the plane of the  $n=11$  (black), 6 (red) and 3 (blue) SLs. (b) Corresponding derivative of the magnetization with respect to temperature obtained from a. The downward arrows indicate the approximate transition temperatures. Inset shows an alloy film of  $\text{La}_{0.35}\text{Eu}_{0.35}\text{Sr}_{0.3}\text{MnO}_3$  (100 uc) in green to compare with the  $n=3$  SL film.

and contained the same composition of LSMO and ESMO, the  $M$ - $T$  exhibits different magnetic features among the three SLs. The  $M$ - $T$  of the  $n = 11$  sample exhibits a kink separating two regimes of magnetic behaviour, a low-temperature transition and a higher temperature transition. Similar behaviour is found in the  $n = 6$  SL film, but the inflection occurs at a higher temperature and the temperature of the second transition is reduced. Interestingly, a divided regime is not observed in the  $n = 3$  SL; instead, only a single transition is apparent.

To quantify this behaviour as a function of temperature, the temperature derivative of the magnetization ( $dM/dT$ ) is shown in Fig. 5b to highlight the distinct transitions. The  $dM/dT$  amplitude from the  $n = 11$  SL (in black) exhibits two minimum points at  $\sim 80$  and  $\sim 315$  K, consistent with the  $T_C$  of ESMO and LSMO films, respectively<sup>37,38</sup>, as supported by the PNR results. Similarly, the  $n = 6$  SL (in red) exhibits two minimum points at  $\sim 105$  and  $\sim 240$  K, indicating the transition temperatures of the ESMO and LSMO are shifted towards one another as the difference in octahedral rotations in the two constituent materials is reduced. In contrast to these, for the  $n = 3$  SL (in blue), the  $dM/dT$  reveals a single minimum point at  $\sim 190$  K, indicating one  $T_C$ . These results demonstrate that the magnetization of the individual layers can be tuned by controlling the magnitude of the rotational modulations throughout the SLs even while the composition of the layers remains unchanged. In the  $n = 3$  SLs, where the distance between interfaces is brought below the interfacial octahedral coupling length, a single  $T_C$  is observed consistent with a uniform octahedral structure despite the presence of the compositional SL. Interestingly, a uniform alloy film of  $\text{La}_{0.35}\text{Eu}_{0.35}\text{Sr}_{0.3}\text{MnO}_3$  (in green) with the same composition as the SLs exhibits significantly reduced  $T_C$  and magnetization compared with the  $n = 3$  SL (inset). We attributed the enhanced  $T_C$  in the SL to the suppression of cation site disorder, as variance in cation size is known to suppress  $T_C$  in bulk manganites<sup>39</sup>.

## Discussion

The transition from a modulated magnetic structure, confirmed by PNR, to a uniform magnetic structure, as indicated by the single transition temperature, is consistent with the structural modulations revealed by STEM and XRD. The STEM imaging reveals a structural coupling length of  $\xi_\theta \sim 4$  uc, a result consistent with the interfacial magnetic width obtained from PNR. As hypothesized, SLs with  $n > \xi_\theta$  behave as the sum of the two constituent materials, whereas the  $n = 3$  SL behaves as a material with uniform magnetization. The observation that the  $T_C$  of the  $n = 3$  sample is between that of bulk LSMO and ESMO is in line with the expectation that the magnitude of the octahedral rotations are approximately the average of those found in LSMO and ESMO. The origin of the switch in rotation pattern with increasing SL period is unknown and will be the subject of future study. Although the  $T_C$  of the LSMO layers is reduced with decreasing  $n$ , the  $T_C$  of the ESMO layers is increased as the layer thickness is reduced: a result not consistent with simple finite thickness effects. However, the increased  $T_C$  of the ESMO layers is fully consistent with an increase in  $\theta$  as  $n$  is reduced. These results directly demonstrate how engineering the local atomic structure of perovskites via the rational design of octahedral superstructures can be used to spatially tailor magnetization in a manner analogous to previous studies utilizing delta doping<sup>12</sup>. However, in this case, it is the local octahedral topology that is altered as opposed to the local electron count or B-site valence. Thus, this work points to new approaches in which ‘structural delta doping’ or rotational gradients are utilized for tuning electronic and ferroic behaviour in multifunctional oxide heterostructures.

## Methods

**Film growth.** Epitaxial SLs were grown on  $(\text{La}_{0.3}\text{Sr}_{0.7})(\text{Al}_{0.65}\text{Ta}_{0.35})\text{O}_3$  (LSAT) (001) substrates by oxide molecular beam epitaxy. An ozone/oxygen mixture ( $\sim 5/95$  %) was used as the oxidizing agent at a chamber pressure of  $\sim 8.5 \times 10^{-6}$  Torr and the temperature of the substrate was kept at  $\sim 600$  °C (refs 37,38). The bulk pseudocubic lattice parameters of the different materials are  $\sim 3.873$  Å (LSMO),  $\sim 3.846$  Å (ESMO) and  $\sim 3.868$  Å (LSAT). LSMO was first grown on a LSAT substrate to minimize strain effects from the substrate. The total thickness of all samples was kept at  $\sim 100$  uc ( $\sim 40$  nm).

**Scanning transmission electron microscopy.** Cross-sectional specimens were prepared using an FEI Helios dual beam focused ion beam/scanning electron microscope using a typical focused ion beam-lift-off approach with final cleaning at a Ga-ion energy of 2 kV (ref. 40). HAADF-STEM imaging and EELS were obtained using a probe-corrected FEI Titan 80–300 operating at 300 kV, equipped with a Gatan QuantumER imaging filter, with nominal energy resolution of  $\sim 0.8$  eV measured by the full-width at half-maximum of the zero-loss peak. The A-site displacement angle was found by averaging the angles of three successive A-site atoms and the error bars represent 0.5 multiplied by the standard deviation of the mean. The atom positions were obtained using ImageJ software from the maximum intensity of each A-site atom following the application of a Gaussian blur filter.

**Synchrotron X-ray scattering.** A systematic survey of the satellite half-order Bragg peaks was carried out on the three SL films at the Advanced Photon Source, Argonne National Laboratory on Sector 33-BM equipped with a two-dimensional PILATUS 100k (single photon counting devices) pixel detector<sup>41</sup>. To resolve the satellite half-order diffraction peaks over the strong and broad background arising from the LSAT diffraction peaks, the data using a PILATUS pixel detector were processed in additional analysis steps using a custom MATLAB algorithm<sup>42,43</sup>. A photon energy of 15.998 keV was used in the measurements. All data were collected at room temperature.

**Polarized neutron reflectivity.** PNR measurements were carried out on the Asterix instrument at LANSCE, Los Alamos National Laboratory. The films were field-cooled to the measurement temperatures with a 5,000-Oe field applied in-the-plane of the films. Measurements were performed in the same field. Data fitting was performed using the NIST Refl1D software package<sup>36</sup>.

## References

- Hwang, H. Y. *et al.* Emergent phenomena at oxide interfaces. *Nat. Mater.* **11**, 103–113 (2012).
- Ohtomo, A., Muller, D. A., Grazul, J. L. & Hwang, H. Y. Artificial charge-modulation in atomic-scale perovskite titanate superlattices. *Nature* **419**, 378–380 (2002).
- Okamoto, S. & Millis, A. J. Electronic reconstruction at an interface between a Mott insulator and a band insulator. *Nature* **428**, 630–633 (2004).
- Popovic, Z. S. & Satpathy, S. Wedge-shaped potential and airy-function electron localization in oxide superlattices. *Phys. Rev. Lett.* **94**, 176805 (2005).
- Lin, C., Okamoto, S. & Millis, A. J. Dynamical mean-field study of model double-exchange superlattices. *Phys. Rev. B* **73**, 041104(R) (2006).
- Bhattacharya, A. *et al.* Metal-insulator transition and its relation to magnetic structure in  $(\text{LaMnO}_3)_{2n}/(\text{SrMnO}_3)_n$  superlattices. *Phys. Rev. Lett.* **100**, 257203 (2008).
- Basletic, M. *et al.* Mapping the spatial distribution of charge carriers in  $\text{LaAlO}_3/\text{SrTiO}_3$  heterostructures. *Nat. Mater.* **7**, 621–625 (2008).
- Yoshimatsu, K., Yasuhara, R., Kumigashira, H. & Oshima, M. Origin of metallic states at the heterointerface between the band insulators  $\text{LaAlO}_3$  and  $\text{SrTiO}_3$ . *Phys. Rev. Lett.* **101**, 026802 (2008).
- Monkman, E. J. *et al.* Quantum many-body interactions in digital oxide superlattices. *Nat. Mater.* **11**, 855–859 (2013).
- Jalan, B., Stemmer, S., Mack, S. & Allen, S. J. Two-dimensional electron gas in  $\delta$ -doped  $\text{SrTiO}_3$ . *Phys. Rev. B* **82**, 081103(R) (2010).
- Kozuka, Y. *et al.* Enhancing the electron mobility via delta-doping in  $\text{SrTiO}_3$ . *App. Phys. Lett.* **97**, 222115 (2010).
- Santos, T. S. *et al.* Delta doping of ferromagnetism in antiferromagnetic manganite superlattices. *Phys. Rev. Lett.* **107**, 167202 (2011).
- Boschker, H. *et al.* Preventing the reconstruction of the polar discontinuity at oxide heterointerfaces. *Adv. Funct. Mater.* **22**, 2235–2240 (2012).
- Bousquet, E. *et al.* Improper ferroelectricity in perovskite oxide artificial superlattices. *Nature* **452**, 732–736 (2008).
- Rondinelli, J. M., May, S. J. & Freeland, J. W. Control of octahedral connectivity in perovskite oxide heterostructures: an emerging route to multifunctional materials discovery. *MRS Bull.* **37**, 261–270 (2012).
- Benedek, N. A., Mulder, A. T. & Fennie, C. J. Polar octahedral rotations: a path to new multifunctional materials. *J. Solid State Chem.* **195**, 11–20 (2012).

17. Torrance, J. B., Lacorre, P., Nazzari, A., Ansaldo, I. E. J. & Niedermayer, C. H. Systematic study of insulator-metal transitions in perovskites  $RNiO_3$  ( $R = Pr, Nd, Sm, Eu$ ) due to closing of charge-transfer gap. *Phys. Rev. B* **45**, 8209(R) (1992).
18. Radaelli, P. G. *et al.* Structural effects on the magnetic and transport properties of perovskite  $A_{1-x}A'_xMnO_3$  ( $x = 0.25, 0.30$ ). *Phys. Rev. B* **56**, 8265 (1997).
19. Takeda, T. *et al.* Metal-semiconductor transition, charge disproportionation, and low-temperature structure of  $Ca_{1-x}Sr_xFeO_3$  synthesized under high-oxygen pressure. *Solid State Sci.* **2**, 673–687 (2000).
20. Imada, M., Fujimori, A. & Tokura, Y. Metal-insulator transitions. *Rev. Mod. Phys.* **70**, 1039 (1998).
21. Jia, C. L. *et al.* Oxygen octahedron reconstruction in the  $SrTiO_3/LaAlO_3$  heterointerfaces investigated using aberration-corrected ultrahigh-resolution transmission electron microscopy. *Phys. Rev. B* **79**, 081405(R) (2009).
22. Borisevich, A. Y. *et al.* Suppression of octahedral tilts and associated changes in electronic properties at epitaxial oxide heterostructure interfaces. *Phys. Rev. Lett.* **105**, 087204 (2010).
23. May, S. J. *et al.* Control of octahedral rotations in  $(LaNiO_3)_n/(SrMnO_3)_m$  superlattices. *Phys. Rev. B* **83**, 153411 (2011).
24. Zhang, J. Y., Hwang, J., Raghavan, S. & Stemmer, S. Symmetry lowering in extreme-electron-density perovskite quantum wells. *Phys. Rev. Lett.* **110**, 256401 (2013).
25. Aso, R., Kan, D., Shimakawa, Y. & Kurata, H. Octahedral tilt propagation controlled by A-site cation size at perovskite oxide heterointerfaces. *Cryst. Growth Design* **14**, 2128–2132 (2014).
26. Fister, T. T. *et al.* Octahedral rotations in strained  $LaAlO_3/SrTiO_3$  (001) heterostructures. *APL Mater.* **2**, 021102 (2014).
27. Tadokoro, Y., Shan, Y. J., Nakamura, T. & Nakamura, S. Crystal structure and characterizations of perovskite oxides  $(Eu,Sr_x)MnO_3$  ( $0.0 \leq x \leq 0.5$ ). *Solid State Ionics* **108**, 261–267 (1998).
28. Mukovskii, Y. M., Hilscher, G., Michor, H. & Ionov, A. M. Magnetic properties, resistivity, and heat capacity of  $EuMnO_3$  and  $Eu_{0.7}A_{0.3}MnO_3$  ( $A = Ca, Sr$ ) compounds. *J. Appl. Phys.* **83**, 7163–7165 (1998).
29. Tomioka, Y., Kumai, R., Ito, T. & Tokura, Y. Magnetic and electronic properties of  $Eu_{1-x}Sr_xMnO_3$  ( $0.3 < x < 0.7$ ) single crystals. *Phys. Rev. B* **80**, 174414 (2009).
30. Zhang, J. Y., Jackson, C. A., Raghavan, S., Hwang, J. & Stemmer, S. Magnetism and local structure in low-dimensional Mott insulating  $GdTiO_3$ . *Phys. Rev. B* **88**, 121104(R) (2013).
31. Glazer, A. M. The classification of tilted octahedra in perovskites. *Acta Crystallogr. B* **28**, 3384–3392 (1972).
32. Glazer, A. M. Simple ways of determining perovskite structures. *Acta Crystallogr. A* **31**, 756–762 (1975).
33. Woodward, P. M. Octahedral tilting in perovskites. I. Geometrical considerations. *Acta Crystallogr. B* **53**, 32–43 (1997).
34. Björck, M. & Andersson, G. GenX: an extensible X-ray reflectivity refinement program utilizing differential evolution. *J. Appl. Crystallogr.* **40**, 1174–1178 (2007).
35. May, S. J. *et al.* Quantifying octahedral rotations in strained perovskite oxide films. *Phys. Rev. B* **82**, 014110 (2010).
36. Kirby, B. J. *et al.* Phase-sensitive specular neutron reflectometry for imaging the nanometer scale composition depth profile of thin-film materials. *Curr. Opin. Colloid Interface Sci.* **17**, 44–53 (2012).
37. Moon, E. J. *et al.* Effect of interfacial octahedral behavior in ultrathin manganite films. *Nano Lett.* **14**, 2509–2514 (2014).
38. Moon, E. J., Keavney, D. J. & May, S. J. Strain effects in narrow-bandwidth manganites: The case of epitaxial  $Eu_{0.7}Sr_{0.3}MnO_3$  thin films. *Phys. Rev. Applied* **1**, 054006 (2014).
39. Rodriguez-Martinez, L. M. & Attfield, J. P. Cation disorder and size effects in magnetoresistive manganese oxide perovskites. *Phys. Rev. B* **54**, R15622(R) (1996).
40. Giannuzzi, L. A., Drown, J. L., Brown, S. R., Irwin, R. B. & Stevie, F. A. Applications of the FIB lift-out technique for TEM specimen preparation. *Micro. Res. Tech.* **41**, 285–290 (1998).
41. Kraft, P. *et al.* Characterization and calibration of PILATUS detectors. *IEEE Trans. Nucl. Sci.* **56**, 758–764 (2009).
42. Schlepütz, C. M. *et al.* Improved data acquisition in grazing-incidence X-ray scattering experiments using a pixel detector. *Acta Cryst.* **A61**, 418–425 (2005).
43. Schlepütz, C. M. *Systematic Structure Investigation of YBCO Thin Films with Direct Methods and Surface X-Ray Diffraction* 189–218 (PhD thesis, University of Zürich, 2009).

## Acknowledgements

E.J.M. and S.J.M. were supported by the US Army Research Office under grant No. W911NF-12-1-0132. Acquisition of the PPMS was supported by the US Army Research Office under grant No. W911NF-11-1-0283. Use of the Advanced Photon Source, an Office of Science User Facility operated for the US Department of Energy (DOE) Office of Science by Argonne National Laboratory, was supported by the US DOE under Contract No. DE-AC02-06CH11357. This work has benefited from the use of Polarized Neutron Reflectometry at the Lujan Center at Los Alamos Neutron Science Center, funded by DOE Office of Basic Energy Sciences. Los Alamos National Laboratory is operated by Los Alamos National Security LLC under DOE Contract DE-AC52-06NA25396. The STEM-EELS was performed at EMSL, a DOE Office of Science User Facility sponsored by the Office of Biological and Environmental Research and located at PNNL.

## Author contributions

Synchrotron X-ray measurements were performed by E.K., E.J.M. and C.M.S. Scanning transmission electron microscopy and electron energy loss spectroscopy were performed by R.C. and analysed by E.J.M. Polarized neutron reflectivity measurements were performed by Q.W. and M.R.F. The XRD and PNR data were fitted, magnetization measurements were performed, and all data were analysed by E.J.M. Samples were prepared by E.J.M. Project was designed and supervised by S.J.M. Manuscript was written by E.J.M. and S.J.M. with contributions by all authors.

## Additional information

**Supplementary Information** accompanies this paper at <http://www.nature.com/naturecommunications>

**Competing financial interests:** The authors declare no competing financial interests.

**Reprints and permission** information is available online at <http://npg.nature.com/reprintsandpermissions/>

**How to cite this article:** Moon, E. J. *et al.* Spatial control of functional properties via octahedral modulations in complex oxide superlattices. *Nat. Commun.* **5**:5710 doi: 10.1038/ncomms6710 (2014).